Lawrence Berkeley National Laboratory

Title

Geodetic monitoring of the geological storage of greenhouse gas emissions

Authors

Vasco, D
Ferretti, A
Rucci, A
et al.

Geodetic Monitoring of the Geological Storage of Greenhouse Gas Emissions

D. W. Vasco[1], A. Ferretti[2], A., Rucci[2], G. Falorni[3], S. V. Samsonov[4], D. White[5], and M. Czarnogorska[4]

1 Energy Geosciences Division, Lawrence Berkeley National Laboratory, University of California, Berkeley, CA

2 TRE ALTAMIRA Srl, Ripa di Porta Ticinese, 79, 20143, Milan, Italy

3 TRE Canada, #410-475 West Georgia Street, Vancouver, British Columbia, Canada

4 Canada Centre for Mapping and Earth Observation, Natural Resources Canada, Ottawa, ON, Canada

5 Geological Survey of Canada, Natural Resources Canada, Ottawa, ON, Canada

Abstract

Geodetic monitoring involves the repeated measurement of the deformation of the Earth. As discussed here, it is a cost-effective approach for inferring reservoir integrity and detecting possible leakage associated with the geological storage of greenhouse gas emissions. Most geodetic methods have favorable temporal sampling, from minutes to months depending upon the technique adopted, and can detect anomalous behavior in a timely fashion. Satellite-based approaches such as Interferometric Synthetic Aperture Radar (InSAR), with their high spatial resolution and broad coverage, are particularly well suited for monitoring industrial scale storage efforts. Multi-temporal analysis, such as permanent scatterer techniques, are improving the accuracy of surface displacement measurements to better then 4-5 mm. New satellites, including the recent X-band systems, are allowing for the routine estimation of two-components of deformation. Data interpretation and inversion techniques may be used to relate the observed displacements to injection-related volume change at depth. InSAR monitoring was used successfully at a gas storage site at In Salah, Algeria where it was determined that the flow in the reservoir was influenced by large-scale fault/fracture zones. InSAR observations are also key components of the monitoring programs at the Aquistore CO_2 storage project in Canada, and the Illinois Basis Decatur Project in the United States. Current InSAR data from both sites indicates no major surface deformation that might be attributed to the stored carbon dioxide, suggesting that the injected fluid remains at depth.

Introduction

Geodetic monitoring, the repeated measurement of displacements and strains, both on the surface and within the interior of the Earth, provides an important class of techniques for assuring the safety of geological storage and for detecting leakage. There are important advantages associated with geodetic methods. The observations are usually gathered frequently in time, from every few minutes to every few months, depending upon the type of data. There are a diverse set of instruments for measuring strain and displacement in various configurations, either on the Earth's surface, at depth, or even from space. Thus, geodetic measurement may often be gather remotely, greatly simplifying data collection and allowing for cost-effective monitoring, particularly in comparison with more intrusive techniques such as seismic surveys. The Earth often deforms in response to fluid injection, particularly at the volumes and rates associated with the geological storage of carbon dioxide. Therefore, geodetic observations are sensitive to fluid volume and pressure changes and may be used to monitor the fate of injected fluids. The magnitude of surface displacement increases dramatically as the source driving the deformation approaches the surface. Thus, geodetic monitoring is well suited to detecting leakage and the upward migration of fluids under pressure. In this Chapter we will discuss the use of geodetic data for monitoring injected carbon dioxide. Our primary focus will be on space-based Interferometric Synthetic Aperture Radar (InSAR) as this is perhaps the most cost-effective geodetic technique for land-based storage sites.

Observational Methods

Overview

Given its practical applications, geodesy, the measurement of distances and changes in distances (displacements) is probably one of the oldest scientific disciplines. Early levelling work and distance measuring techniques involving the use of calibrated rods and chains date back to ancient times and continue to this day, though they have largely been replaced by satellite- and laser-based techniques. Another early technique was the measurement of the local slope, the horizontal gradient of surface elevation, using a calibrated bubble level. This has evolved to modern day, highly accurate, capacitance-based tilt meters, capable of determining angular changes with nano-radian precision (Wright 1998), optical fiber tilt meters (Chawah et al. 2015), and portable tilt meters and extensiometers (Hisz et al. 2013). Advanced tilt meters are now self-leveling and may

be used in boreholes and on the seabed. Trilateration by a constellation of satellites is the basis for the Global Positioning System (GPS), and Global Navigation Satellite Systems (GNSS) in general. This technology appears in many applications including the monitoring of subsurface fluid flow (Moreau and Dauteuil 2013). Both tilt and GNSS measurements usually have high temporal resolution, with observations gathered every few minutes or hours (Schuite et al. 2017). However, cost often constrains one to a sparse network of instruments, limiting the spatial resolution of the displacement field. Leveling is similarly restricted to point measurements, typically gathered along roads or other open areas.

There is another class of observation techniques that can best be described as scanning systems. In these devices propagating waves are reflected off objects of interest and the returns are used to estimate distances. Most commonly electromagnetic waves are utilized. However, there are also sonar (sound waves) and seismic (elastic waves) systems that are used in particular applications. For example, time-lapse seismic surveys have been used to extract seismic time strains over deforming reservoirs, a measure of the vertical strain in the subsurface. Such a technique has the advantage that the wave is sensing displacements at depth and even within the reservoir. Such displacements will typically be much larger then surface displacements. Shortly after the invention of the Laser the phase shift of its signal was used to measure changes in distance. Such laser ranging has progressed and is now used over a wide range of scales from engineering applications to airborne LiDAR surveys and even satellites (Eitel et al. 2016) and is useful for mapping geologic hazards (Joyce et al. 2014). Longer wavelength microwave signals are used in InSAR imaging, perhaps the most promising geodetic technology for monitoring the geological storage of carbon dioxide (Massonnet and Feigl 1998, Rosen et al. 2000, Ferretti 2014). In the next section we describe this approach in much more detail. In the Applications section we illustrate the use of InSAR observations at three storage sites.

SAR Interferometry

Radar sensors mounted on satellite platforms, airplanes, or even a tripod on the ground, make it possible to measure ground displacement with millimeter accuracy, thanks to a particular technique known as SAR (Synthetic Aperture Radar) interferometry (InSAR) [see Ferretti (2014) for a comprehensive review]. The satellites both send and receive signals, recording the complex returns and using them for both imaging and range (distance) estimation (Figure 1). Unlike optical systems, the sensors operate in the microwave domain, with wavelengths of a few centimeters, 100,000 times longer than those of the visible spectrum. Being an active system, a radar sensor can function 24 hours a day and year-round, as it can see through clouds, fog and rain, independently of the Earth's illumination.
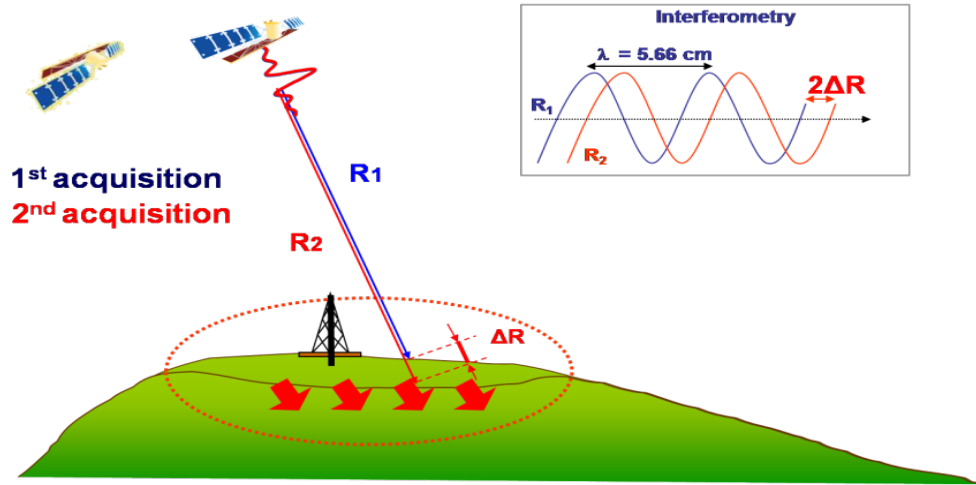
Figure 1: A schematic showing the relationship between ground displacement and signal phase shift. The numeric value of the wavelength λ, is that used by the ERS satellites operated by the European Space Agency (ESA).

An important feature of a SAR system is its ability to record both amplitude and phase information. While the amplitude depends on the amount of energy backscattered towards the sensor, the phase is related to the distance between the phase center of the radar antenna and the target on ground. More precisely, the phase value φ of a pixel P of a radar image can be modeled as a mixture of four distinct contributions (Ferretti et al. 2007a, Rosen et al. 2007):

$$\varphi(P) = \vartheta + \frac{4\pi}{\lambda}r + a + n \quad (1)$$

where ϑ is the phase shift related to the location and to the reflectivity of all elementary scatterers within the resolution cell associated with pixel P. The coefficient $\frac{4\pi r}{\lambda}$ is the most significant contribution in any geodetic application, as it is associated with the sensor-to-target distance r. The term a is a delay introduced by the medium (the Earths atmosphere) that the electromagnetic wave propagates through. This quantity, known as the *atmospheric phase screen* (APS), is often the main source of noise and can compromise the quality of any distance estimate. The last term, n, is a phase contribution related to system noise (thermal noise, quantization, etc.).

The phase values contained in a single SAR image are of little practical use, as it is impossible to separate the different contributions in equation (1), at least without prior information. The basic idea of SAR interferometry is to measure the phase *change*, or interference, over time, between two radar images, generating an *interferogram I*:

$$I = \Delta \varphi(P) = \Delta \vartheta + \frac{4\pi}{\lambda}\Delta r + \Delta a + \Delta n \qquad (2)$$

If we consider an idealized situation where the noise is negligible, the surface character (reflectivity) and atmospheric conditions are constant between the two SAR acquisitions, then equation (2) reduces to

$$I = \Delta \, \varphi(P) = \frac{4\pi}{\lambda} \Delta r. \qquad (3)$$

Therefore, if a point on the ground moves during the time interval between the acquisition of the two radar images with similar geometry, the distance between the sensor and the target changes, creating a phase shift proportional to the displacement (Figure 1). Equation (3) explains why inteferometric SAR techniques can measure range variations with high sensitivity: the unit of length of the measurement is the wavelength (a few centimeters long) rather than the range resolution of the radar sensor (typically a few meters). A displacement of the radar target by a distance of $\lambda/2$ will create a phase shift of 2π radians. Therefore, a range variation of just 1 mm creates a phase shift of more than 20 degrees between two SAR images acquired in the X-band ($\lambda=3$ cm), which can be easily detected.

A direct approach, involving the computation of phase variations on a pixel-by-pixel basis between two radar images, can only be used successfully if the reflective character of the radar target does not change over time, the signal-to-noise-ratio (SNR) is high enough, and the atmospheric phase components are negligible. When this is not the case the analysis of a single interferogram is not sufficient to produce useful estimates and a *multi-interferogram* approach is required. In fact, the analysis of *long temporal series* of SAR images, as described in the next sub-section, is perhaps the best way to disentangle the different phase contributions and retrieve high quality displacement data.

Multi temporal analysis

Techniques utilizing a suite of interferograms, multi-interferogram approaches, are aimed at overcoming limitations associated with phase de-correlation and atmospheric effects. The PSInSAR technique (Ferretti et al. 2000, Ferretti et al. 2001), developed in the late nineties, initiated a 'second generation' of algorithms addressing the difficulties related to conventional (single-pair) analyses. The basic idea is to compare many SAR images and to focus the analysis on high quality radar targets, usually referred to as Permanent Scatterers (PS). Such targets exhibit very stable radar signatures and allow the implementation of powerful filtering procedures to estimate and remove atmospheric disturbances, so that extremely accurate displacement data can be estimated. Common to all geodetic applications, the displacements are computed with respect to a stable reference point.

A recent enhancement of the permanent scatterer technique, the SqueeSAR algorithm [Ferretti et al. 2011], allows for two families of stable points on the Earth's surface, permanent scatterers and distributed scatterers.

As noted above, permanent scatterers (PS) are radar targets that are highly reflective (backscatter significant energy), generating very bright pixels in a SAR scene. Permanent scatterers are associated with stable features such as buildings, metallic objects, pylons, antennae, outcrops, etc. Distributed scatterers (DS) are radar targets usually comprised of a localized collection of pixels in the SAR image, all exhibiting a very similar radar signature. Such scatterers usually correspond to rocky areas, detritus, and areas generally free of vegetation. Temporal de-correlation, though still present in distributed scatterers, is small enough to allow for the retrieval of their displacements. Provided enough SAR images are available, one can determine a time series of range change (displacement along the line of sight) regardless of the type of scatterer identified by the algorithm. Thus, estimates of the geographic coordinates of the measurement point (located with a precision of about 1 m), average annual velocity of the measurement point (with a precision dependent on the number of data available, but typically less than 1 mm/yr), and time-series of scatterer displacement (with a precision typically better than 4-5 mm for individual measurements).

In order to successfully perform a multi-interferogram analysis, a minimum number of satellite images (approximately 10-15) are required. This is necessary to create a reliable statistical analysis of the radar returns, making it possible to identify pixels that can be used in the analysis. The higher the number of images acquired and processed, the better the quality of the results. For displacement data associated with permanent and distributed scatterers, a key factor is the distance from the reference point. The relative accuracy can be better than a few millimeters for a distance less than the average correlation length of the atmospheric components (about 4 km at mid-latitudes). Average displacement rates can be estimated with a precision better than 1 mm/yr, depending on the number of data available and the temporal span of the acquisitions (Ferretti 2014).

Two-Dimensional Displacement Decomposition

Satellite SAR interferometry only measures the projection of the three-dimensional displacement vector along the satellite line-of-sight. The data from any given interferogram are therefore, single component distance measurements. However, it is possible to combine radar data acquired from different acquisition geometries to approximate two-dimensional displacement fields (Rucci et al. 2013). In fact, all SAR sensors follow near-polar orbits and every point on Earth can be imaged by two different acquisition geometries: one with the satellite flying from north to south (descending mode), looking westward (for right-looking sensors) and the other with the antenna moving from south to north (ascending mode), looking eastward. This is the reason why, by combining InSAR results from both acquisition modes, it is possible to estimate two components of displacement.

To illustrate how the decomposition is performed, imagine a Cartesian reference system, where the three axes correspond to the East-West (X), North-South (Y) and Vertical direction (Z). Consider the case in which two estimates of the target range change are available, obtained from both ascending and descending radar acquisitions, namely r_a and r_d (Figure 2). In the Cartesian reference system X-Y-Z, the range change of a scatterer on ground can be expressed as:

$$r = d_x \cdot l_x + d_y \cdot l_y + d_z \cdot l_z \qquad (4)$$

where d_x, d_y and d_z represent the component of the displacement $\vec{d}$ along the E-W, N-S and vertical directions, and l_x, l_y, l_z are the direction cosines of the look vector.
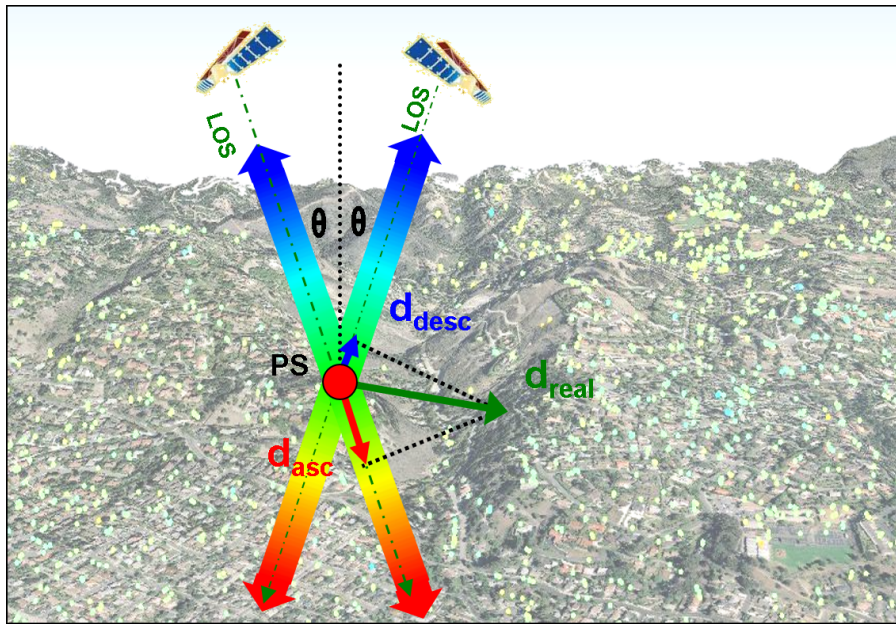
Figure 2: Example of motion decomposition combining ascending and descending acquisition geometry

Given our knowledge of the satellite orbit, the line of sight of the radar antenna is known, as are the corresponding direction cosines of the velocity vector r_a and r_d. It is thus possible to write the following system of equations:

$$\begin{bmatrix} r_a \\ r_d \end{bmatrix} = \begin{bmatrix} l_{x,a} & l_{y,a} & l_{z,a} \\ l_{x,d} & l_{y,d} & l_{z,d} \end{bmatrix} \cdot \begin{bmatrix} d_x \\ d_y \\ d_z \end{bmatrix} \qquad (5)$$

where $l_{x,a}$, $l_{y,a}$, $l_{z,a}$ and $l_{x,d}$, $l_{y,d}$, $l_{z,d}$ are the direction cosines of the satellite line of sight for both ascending and descending acquisitions. The problem is poorly posed if we now want to invert for the full three-

dimensional velocity vector, as there are three unknowns (d_x, d_y and d_z) and only two equations. However, because the satellite orbit is almost circumpolar, the sensitivity to possible motion in the north-south direction is negligible (the direction cosines $l_{y,a}$ and $l_{y,d}$ are close to 0). This allows us to rewrite the system in the following form:

$$\begin{bmatrix} r_a \\ r_d \end{bmatrix} \approx \begin{bmatrix} l_{x,a} & l_{z,a} \\ l_{x,d} & l_{z,d} \end{bmatrix} \cdot \begin{bmatrix} d_x \\ d_z \end{bmatrix} , \quad (6)$$

an equation that may be solved for d_x and d_z.

Data Interpretation and Inversion Methods

When a volume of fluid is introduced under pressure at some depth within the Earth it changes the state of rock-fluid system around the injection site. The nature of the change is determined by the temperature, composition, pressure, and flow rate of the fluid and the initial conditions within the host formation. Generally, the injected fluid will displace the in-situ fluid, leading to pressure and consequently volume changes that depend on the compressibility of the system as a whole. These volume changes will lead to strain within the Earth that will be transmitted outward from the injection site, ultimately reaching the Earth's surface. Given sufficient strain at depth, the resulting surface displacement can be large enough to produce a significant signal, observable by modern geodetic instruments such as a SAR satellite. Such signals can produce valuable information concerning the source of the deformation.

Given an observable pattern of surface deformation, one can attempt to infer properties of the source generating the deformation. That is, one can invert the observed data to estimate parameters describing the source. One to the most important aspects of an inversion for volume change is the parameterization of the source model. In order to effectively represent the source, one must know its basic geometrical properties and boundary conditions. For example, if the injected fluid is confined to a porous layer then it is important to include the impermeable boundaries of the layer. Or if the injected fluid induces the opening of a tensile fracture then the strike and dip of the feature will need to be specified, perhaps by a data fitting procedure. For a tensile fracture the volume change is completely determined by the aperture change over the fracture. Thus, the nature of the elemental source will be different from the volume expansion of a grid block. In fact the expansion of a grid block can be modeled by three orthogonal tensile fractures, one along each axis. Other, more complicated source combinations are possible, such as slip induced along a tensile fracture. A correct formulation of the problem requires knowledge of the geology as well as of the general stress conditions at depth. Furthermore, one must be willing to modify the formulation in light of new information. For example,

at In Salah a double lobed pattern of surface deformation indicated a tensile feature at depth, giving rise to a modified source model.

 Under favorable circumstances, surface deformation may be used to image the migration of the injected and displaced fluid at depth and the geological features that are controlling it. Needless to say, making such inferences will require knowledge of the properties of the fluids involved and of the overburden. However, the nature of the injected fluid is usually well known and the structure and properties of the overburden are also constrained by seismic data and well logs. One does not typically inject fluid blindly into the Earth. For the sake of our discussion we will assume that the Earth behaves elastically at a sufficient distance from the source and for the time intervals in question, a few months to a few years. Furthermore, we will assume that the elastic properties can be reasonably estimated from the available data. Other rheological models, such as viscoelasticity, are certainly possible and are not a barrier to the approach that we shall lay out here. However, for the conditions associated with the geological storage of greenhouse gases, an elastic overburden is a reasonable model.

Geodetic methods do not really allow us to image fluid flow directly. In particular, displacements at the surface and within the overburden are responding to the effective volume changes induced by fluid injection and withdrawal.   Imagine a box around that part of the reservoir influenced by fluid injection or withdrawal. If we cut out the reservoir and simply applied the same displacements as those caused by the fluid flow to the boundaries of the box, the resulting deformation in the overburden, and on the surface, would be the same. So, in reality, one can only solve for such effective displacements or volume changes. Other assumptions, such as constitutive laws for the reservoir, are required if we are to interpret the volume changes in terms of fluid pressure changes, thermal expansion, or non-elastic processes. Therefore, we will formulate our inversion in terms of reservoir fractional volume change in order to minimize the number of assumptions that must be invoked.

In an elastic Earth the displacement at the surface, and in the overburden, is linearly related to the volume changes within the source region (Aki and Richards 1980, Vasco et al. 1988). Thus, one can write the calculated displacements as an integral over with source volume V

$$u_i(\boldsymbol{x}) = \int_V G_i(\mathbf{x}, \boldsymbol{y}) \Delta v(\boldsymbol{y}) d\boldsymbol{y} \qquad (7)$$

where $\Delta v(\boldsymbol{y})$ is the fractional volume change at source location $\boldsymbol{y}$. The quantity $G_i(\mathbf{x}, \boldsymbol{y})$ is a Green's function representing the i-th displacement component at location $\mathbf{x}$ that results from a point volume increase at $\mathbf{y}$. The Green's function encapsulates the physics of the propagation of elastic deformation from the source to the observation point, obtained by solving the governing equation with a point source. For a simple medium with

sufficient symmetry, such as a homogeneous half-space it is possible to produce an analytic Green's function. For a more general medium one must resort to numerical approaches in order to compute $G_i(\mathbf{x}, \mathbf{y})$. Even a layered medium requires a numerical approach to compute the Green's function (Wang et al. 2006).

Equation (7) constitutes the forward problem whereby the injected volume is specified and the displacement at the observation points are calculated. For computational purposes the source volume is usually decomposed into a discrete sum of N elementary volumes, such as rectangular grid blocks, and the total volume has the basis function representation

$$V = \sum_{j=1}^{N} V_j. \qquad (8)$$

Note that the volumes may be taken to be quite small and sources are often decomposed into one or more point-like sources. Substituting the volume expansion (8) into the integral (7), and using the linearity of integration, results in the expression

$$u_i(\mathbf{x}) = \sum_{j=1}^{N} G_{ij}(\mathbf{x}) \Delta v_j. \qquad (9)$$

It is assumed that the fractional volume change given by Δv_i, is constant over the elemental volume V_j. The function $G_{ij}(\mathbf{x})$ represents the integral of the Green's function $G_i(\mathbf{x}, \mathbf{y})$ over V_j

$$G_{ij}(\mathbf{x}) = \int_{V_j} G_i(\mathbf{x}, \mathbf{y}) d\mathbf{y}. \qquad (10)$$

For InSAR observations the data will consist of range change values, given by the projection of the displacement vector onto the satellite look vector $\mathbf{l} = (l_1, l_2, l_3)$. Thus, the range change will be given by $r = \mathbf{l} \cdot \mathbf{u}$ and the projection applied to equation (9) gives

$$r(\mathbf{x}) = \sum_{j=1}^{N} M_j(\mathbf{x}) \Delta v_j, \qquad (11)$$

where the range change kernel $M_j(\mathbf{x})$ is

$$M_j(\mathbf{x}) = \sum_{i=1}^{3} l_i G_{ij}(\mathbf{x}). \qquad (12)$$

If we write the collective range change data for all of the pixels as a vector $\mathbf{r}$, then the corresponding set of linear constraints, each in the form of equation (11), may be written as a matrix equation

$$\mathbf{r} = \mathbf{M}\mathbf{v}. \qquad (13)$$

In the inverse problem observational data are used to estimate the distribution of volume change at depth. The most common approach is a least squares formulation in which one seeks a model $\mathbf{v}$ that minimizes the sum of the square of the residuals

$$S = (\mathbf{r} - \mathbf{Mv})^t \cdot (\mathbf{r} - \mathbf{Mv}) . \qquad (14)$$

While it is possible to try and estimate the volume change for a full three-dimensional source model by minimizing S, the solution will most likely be non-unique or poorly determined. That is, there will be many possible solutions and solving the least squares constraint equations will not lead to a stable answer. One can stabilize the solution by adding penalty terms to the misfit function S, representing aspects of the model that are considered undesirable, a procedure known as regularization. For example, the magnitude of deviations from an initial or prior model,

$$M = (\mathbf{v} - \mathbf{v_0})^t \cdot (\mathbf{v} - \mathbf{v_0}) \qquad (15)$$

is often included as a penalty term. A term penalizing model roughness is also commonly used to regularize the inverse problem. Note that if one takes $\mathbf{v_0}$ equal to zero, the norm penalty will have the undesired effect of biasing the solution to have the largest changes at the shallowest depth. That is, in order to minimize the magnitude of the solution, most significant anomalies are placed close to the surface, where they will have the greatest effect on the observations.

Given fluid injection and production data, it is often useful is to constrain the changes in particular formations to try and honor the fluid volume information in addition to fitting the geodetic data. For example, given the net injected volumes, v_i, in a specific set of grid blocks B_I, we can add the penalty term

$$I = \sum_{i \in B_I} (\mathrm{v}_i - f v_i)^2 \qquad (16)$$

to the data misfit function S, *where f is a scaling factor to account for the fact that the injection of a cubic meter of water leads to a change that is a fraction of the injected volume.* If no such information is available, or if one is uncertain on how to scale the injected fluid volume to fractional volume changes at depth, it is still possible to penalize changes that are far from the well. That is, we can bias the solution to try and put the most significant volume changes near the injection site, where the pressure changes should be the largest. For example, if a well is located at $\mathbf{x}_w$ then the penalty function takes the form

$$D = \sum_{i=1}^{N} \Delta(\mathbf{x}_w, i) \mathrm{v}_i^2 \qquad (17)$$

where $\Delta(\mathbf{x}_w, i)$ is a function measuring the distance between the well and the center of the i-th grid block.

One of the advantages of geodetic observations is the relatively dense temporal sampling in comparison to other geophysical methods. For example, SAR data may be gathered at weekly to monthly intervals, leading to a time series of range change for each scatterer. Hence, it is possible to image the time evolution of the

volume changes and to try and relate these changes to fluid movement and hydrological properties such as permeability (Vasco 2004, Vasco et al. 2008, Rucci et al. 2010). The sequence of volume changes within each grid block of the reservoir model can be used to estimate an arrival or onset time, that moment at which the volume of a grid block is changing most rapidly. As discussed in Vasco et al. (2008) the onset time can be related to the travel time of the pressure front initiated by the start of injection. Specifically, for an elastic medium and a sharp injection profile resembling a step-function, the onset of the peak rate of volume change, T_{peak}, is related to the phase σ of the propagating pressure front according to $\sigma = \sqrt{6T_{peak}}$ (Vasco et al. 2000). For propagation governed by the diffusion equation, the phase is given by the solution of an eikonal equation

$$\nabla\sigma \cdot \nabla\sigma - \gamma = 0, \qquad (18)$$

where $\gamma(\mathbf{x})$ is the inverse of the hydraulic diffusivity (Vasco et al. 2000, Vasco and Datta-Gupta 2016, p. 138) . The nonlinear, first-order eikonal equation is equivalent to the system of ordinary differential equations

$$\frac{d\mathbf{x}}{ds} = \nabla\sigma \qquad (19)$$

$$\frac{d\sigma}{ds} = \sqrt{\gamma} \qquad (20)$$

where $\mathbf{x}(s)$ is the flow path in the porous medium and s is the distance along the path. These expressions may be used to find the hydraulic diffusivity, and consequently the effective permeability, within the reservoir. As was shown by Rucci et al. (2010), permeability estimates based upon diffusive travel times are primarily sensitive to the kinematics of the pressure propagation and not sensitive to the coupling between the magnitudes of reservoir pressure and volume change.

Field Applications

In this section we describe three large-scale CO_2 storage projects that made, or are making, use of geodetic monitoring. All three projects incorporated InSAR observations into their monitoring workflow.

In Salah, Algeria

At In Salah, Algeria excess carbon dioxide from the production at three gas fields was removed, processed, and re-injected into the flanks of an anticline defining one of the fields. The target reservoir for long-term storage was a sandstone layer roughly 20 m thick, overlain by almost 1 km of shales and siltstones and an additional kilometer of inter-bedded sandstones and shales. Initially, it was supposed that the carbon dioxide would simply reside in the reservoir. Since the start of injection in 2004, roughly 3.8 million tonnes of carbon dioxide have been sequestered. Initial predictions of surface uplift, obtained from coupled hydrological-

geomechanical simulations, varied from a few millimeters to about one centimeter (Rutqvist et al. 2010, Bissell et al. 2011). InSAR data acquisition was part of an extensive monitoring effort devised by the partners of a Joint Industry research and development program (Mathieson et al. 2010, Ringrose et al. 2013). Several of the monitoring activities, including micro-seismic and InSAR data collection, were in collaboration with Lawrence Berkeley National Laboratory. Fortunately, the surface conditions at the In Salah site are quite favorable to SAR monitoring and the permanent scatterer approach, with a boulder strewn, hard packed surface, and a restricted supply of mobile sand. The project benefited by both large-scale (Bissell et al. 2011) and detailed coupled modeling of the flow and related geomechanics (Rutqvist et al. 2010).

Envisat Range Change Observations

For the first phase of this work Lawrence Berkeley National Laboratory contracted TRE to process existing data in the European Space Agency Envisat archive from July 12, 2003 to March 19, 2007. Two satellite tracks covered the region containing the three injection wells, Tracks 65 and 294. During this initial study period the respective tracks contained 26 and 18 satellite images, with one or more months between each image. The data were processed using the permanent scatterer algorithm described above. The range change data for both tracks provided an estimate of ground displacement along the line-of-sight of the satellite, that is, along the look direction of the satellite. The analysis of the Envisat data revealed observable surface deformation associated with the injection of carbon dioxide. Peak velocities of over 5 mm/year were found for both tracks, exceeding the estimated errors of 1 mm/year. Elongated patterns of range decrease were imaged, suggesting uplift over the three injection wells KB-501, KB-502, and KB-503 (Figure 3).
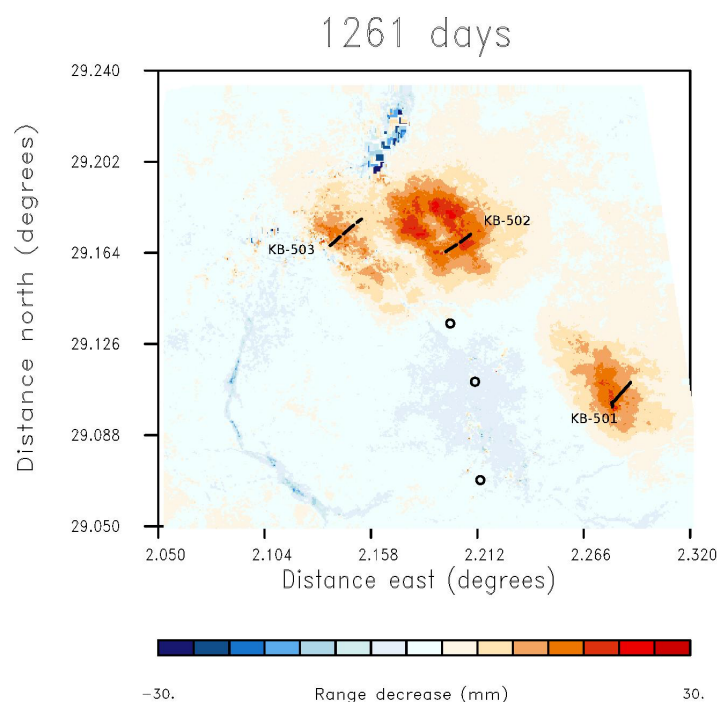
Figure 3: Range changes above the carbon storage site at In Salah, Algeria, 1261 days after the start of injection. The black lines are the traces of the injection wells within the target formation. The open circles denote the wellhead locations of the gas producers.

Initially, the range decreases in the region overlying the well KB-501 were assumed to be the result of injection related volume change within the reservoir (Vasco et al. 2008). Following the procedure described above [see equation (11)] the reservoir volume surrounding the injector was mapped into a grid of cells. A regularized least-squares approach was used to estimate the fractional volume changes within each grid block. A mapping of the sequence of range change into reservoir volume change in the region surround well KB-501 indicated preferential migration to the northwest of the injection well. Using the diffusive imaging technique describe above, the propagation times of the volume changes were used to calculate permeability variations within the reservoir layer (Vasco et al. 2008).
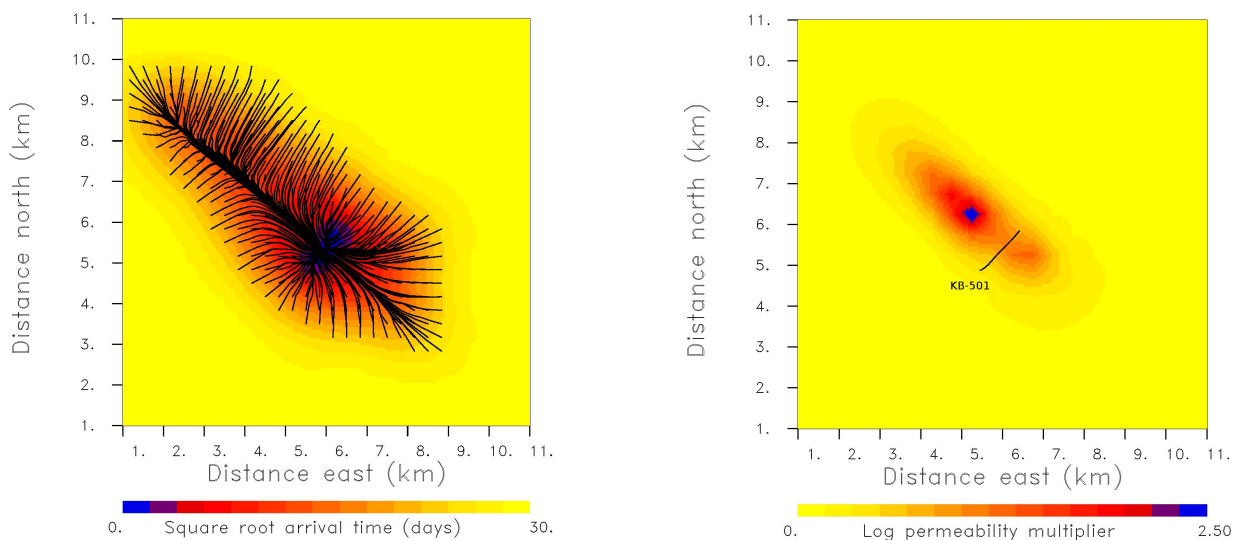

Figure 4: (Left panel) Onset time of the most rapid change in reservoir volume. The curves indicate the flow paths from the well to points within the reservoir and are calculated by solving equation (19). (Right panel) Logarithm of the permeability multiplier found by solving equation (20) along the trajectories.

Specifically, the time series of volume changes for each grid block were used to define the onset of the peak rate of change T_{peak}. This time is related to the phase of the propagating front σ, according to $\sigma = \sqrt{6T_{peak}}$ (Vasco et al. 2000). In Figure 4 the variations in the phase are plotted for those regions where the volume changes were significant. The trajectories are found by solving equation (19). The solution is quite simple

because the right-hand-side is the known phase field σ. So the trajectories are found by marching down the gradient from each grid block center back to the well. Given the trajectories and the spatial distribution of σ one can estimate the diffusivity by solving equation (20) for γ. This is a tomographic problem of a slightly different nature then that of cross-well imaging. For the problem at hand, there are many trajectories traveling along a similar flow path but for varying distances. The density of trajectories sampling the flow path depends upon the temporal sampling provided by the geodetic data. Thus, one can incrementally build up the diffusivity distribution along each flow path, based upon the set of trajectories sampling that path. The resulting permeability estimates indicated a narrow, northwest-trending corridor of higher permeability (Figure 4). The correlation of this high permeability feature with a northwest trending break in seismic topography suggested that the carbon dioxide injected into well KB-501 might flow preferentially along a fault zone on the flank of the anticline defining the field (Vasco et al. 2008).
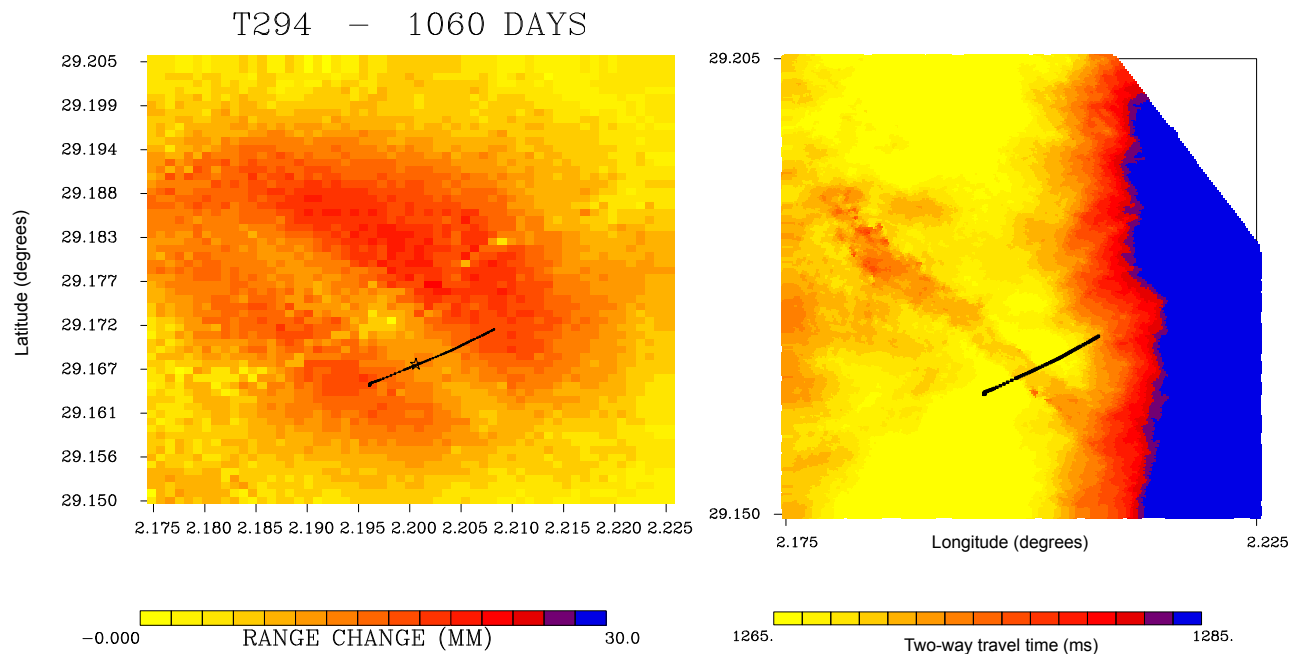

Figure 5: (Left panel) Detailed view of range change above well KB-502 following 1060 days of injection. The darker colors signify range decrease associated with uplift above the well. (Right panel) Seismic horizon displaying push-down, most likely due to velocity decreases associated with the migration of injected carbon dioxide.

The range changes observed over injector KB-502 displayed a distinct double-lobed pattern seen in Figures 3 and 5 (Vasco et al. 2010). As noted by collaborators from Pinnacle Technologies, such patterns were often observed in tilt meter monitoring of hydro-fracturing, suggesting the tensile opening of a steeply-dipping planar feature (Davis 1983). For a tensile feature, such as a fracture, the fluid pressure induces the fracture to open. Thus, the volume change is primarily due to displacement normal to the fracture plane, a change in

fracture aperture (fracture width). On the basis of Pinnacle's suggestion, a vertical to sub-vertical fault/fracture zone model was constructed. The zone extended 80 m above and below the reservoir and approximately 6 km to the northwest and 6 km to the southeast of the injection point in the plane, trending on an azimuth of 135 degrees. In addition, volume change within the reservoir layer was also accounted for in the fashion described above (Vasco et al. 2010).

A homogeneous elastic model of the overburden did not produce the correct range change estimates and hence an inversion based upon a model with uniform properties led to erroneous depth estimates for a tensile source. Thus, elastic layering, derived from well logs, had to be included in the modeling. The total range change from July 12, 2003 through March 19, 2007 was used to infer the distribution of volume change within the reservoir and the distribution of aperture change over the fault/fracture zone. It was found that the range changes could be matched by a combination of reservoir volume change and cumulative tensile opening of a fault/fracture zone confined to lie at depths within 100 m of the reservoir (Vasco et al. 2010). The lateral extent of the fracture opening was much greater, extending over three kilometers from the injection point. Aspects of the fault/fracture zone were subsequently supported in an analysis of three-dimensional surface seismic data. In particular, Gibson-Poole and Raikes (2010) noted that time shifts, thought to be due to the injection of carbon dioxide and the resulting seismic velocity change, followed a remarkably linear zone with near parallel boundaries and located between the two lobes of range change (Figure 5). The orientation of the seismic feature agreed rather well with the azimuth of 135 degrees required to fit the range change data. These conclusions were subsequently supported by the work of Zhang et al. (2015, 2016).

X-Band InSAR and Multi-Component Displacement Data

The Envisat C-band satellite was deorbited on October 2010 and no longer available for monitoring the range changes over the injectors at In Salah. Fortunately, several other satellite systems were functional as replacements before this date. In particular, the COSMO-SKymed (CSK) X-band satellite pair were launched and operational before the loss of the Envisat satellite. Similar, the TerraSAR X-band satellite was also put in orbit, with a repeat cycle of 11 days. Thus, three X-band satellites were accessible for estimating range changes at the In Salah site due to the injection of carbon dioxide. The repeat time attainable for these three satellites was 8 to 11 days, much better then the best possible Envisat return time of 35 days. The down side of this transition to X-band data was the increased cost of data acquisition because the satellites have to be tasked to gather data at a particular site. However, with the help of British Petroleum, we were able to acquire X-band SAR scenes from both ascending and descending acquisition geometries from 2009 until 2012.
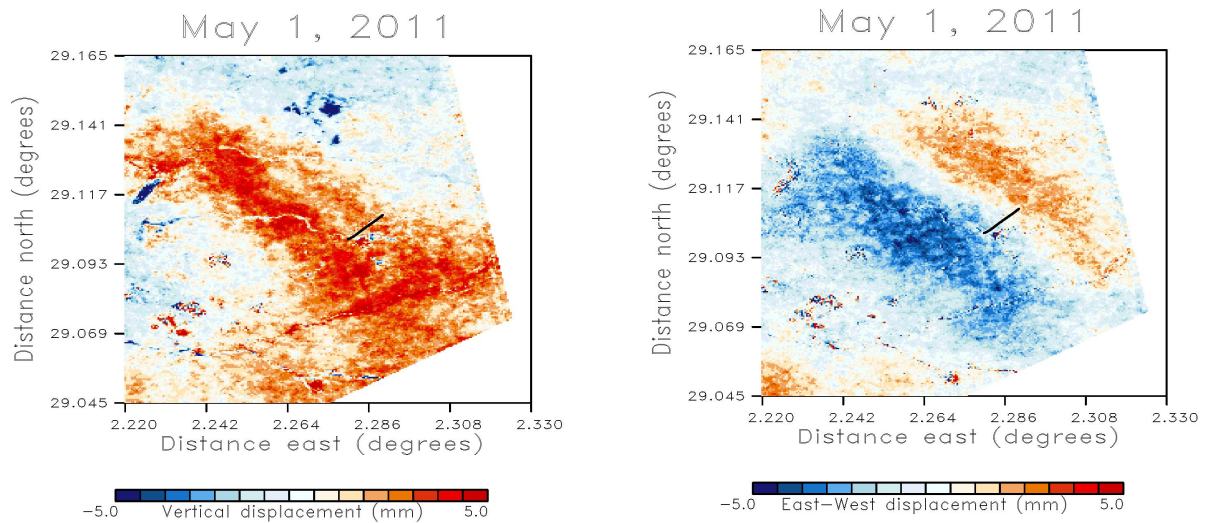
.

Figure 6: (Left panel) Vertical displacements above well KB-501, derived from X-band InSAR data. (Right panel) East-west displacements above the injection well KB-501.

Due to the favorable geometry of the two satellite systems it was possible to obtain both quasi-east-west and quasi-vertical components for all time intervals during this period. An example is shown in Figure 6 for displacements above well KB-501. Note that there is a hint of a double lobed pattern in the vertical component of displacement. As at KB-502, this pattern suggests the possible opening of a sub-vertical tensile feature, such as a fault or damage zone. The existence of such a damage zone is supported by the narrow, linear, high-permeability trend shown in Figure 4, found by in the diffusive travel time inversion of Vasco et al. (2008). Furthermore, a recent inversion of a decomposition of C-band data into quasi-vertical and quasi-east-west components found that is was not possible to fit both data sets simply with reservoir volume change. A contribution from a sub-vertical tensile feature provided an acceptable fit to the two components (Rucci et al. 2013). Based upon these results, a steeply-dipping (86°) tensile damage zone model was adopted to explain the surface displacement observed in Figure 6. The sub-vertical damage zone, with an orientation of 135°, was divided into a 20 by 15 grid of surface elements. Each grid element could undergo a distinct aperture change in order to fit the two components of data. The resulting model (Figure 7) contains an elongated region of aperture change from the depth of injection to about 100 m above the well. Significant aperture change extends roughly 6 to 7 km to the northwest of the injection well and about 5 km to the southeast.
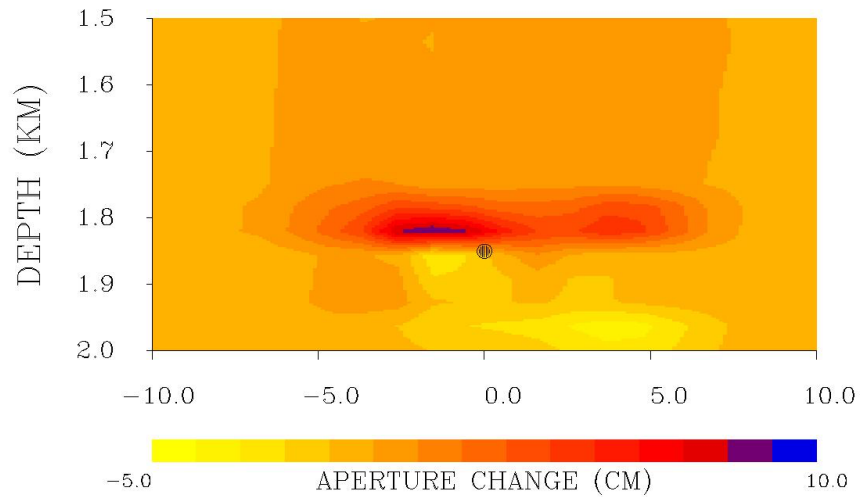
Figure 7: Distribution of total aperture change (effective fracture zone opening) on a dipping damage zone, produced by an inversion of the two components of displacement shown in Figure 6. The black dot denotes the intersection point of the horizontal well with the damage zone.

The aperture change estimates, shown in Figure 7, provide a reasonable fit to the InSAR observations, even reproducing the small secondary lobe at the eastern edge of the vertical displacement anomaly (Figure 8).
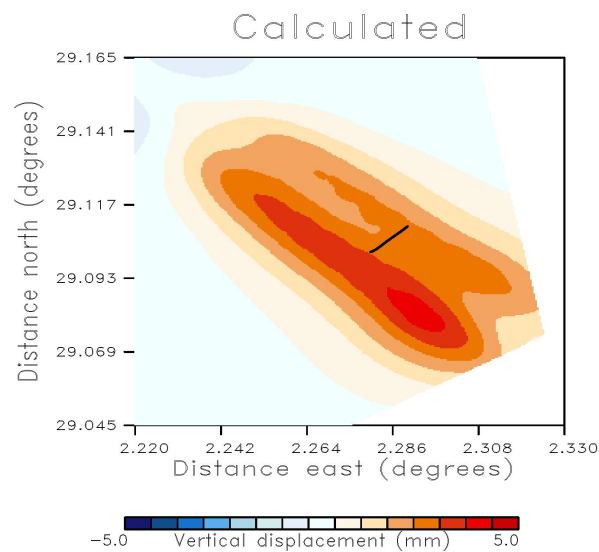

Figure 8: Calculated vertical displacement based upon the distribution of aperture change plotted in Figure 7.

Aquistore, Canada

The Aquistore CO_2 Storage Project (Worth et al., 2014) began in 2012 in southeastern Saskatchewan, Canada (Figure 9). The site serves as buffer storage for the world's first commercial, post-combustion, carbon capture plant that began operation in October 2014 at the Boundary Dam coal-fired power station. Injection started in April 2015 with a maximum anticipated injection rate of up to 1500 tonnes/day. The carbon dioxide is sequestered in the brine-filled clastic strata of the Deadwood and Winnipeg formations at 3150-3350 m depth, the deepest sedimentary units in the Williston Basin (Norford et al., 1994). Similar deep saline formations are found throughout the world. These formations are well suited for the storage of carbon dioxide because they are porous and permeable, have huge volumes, and are overlain by geologic seals that will impede the upward migration of CO_2.
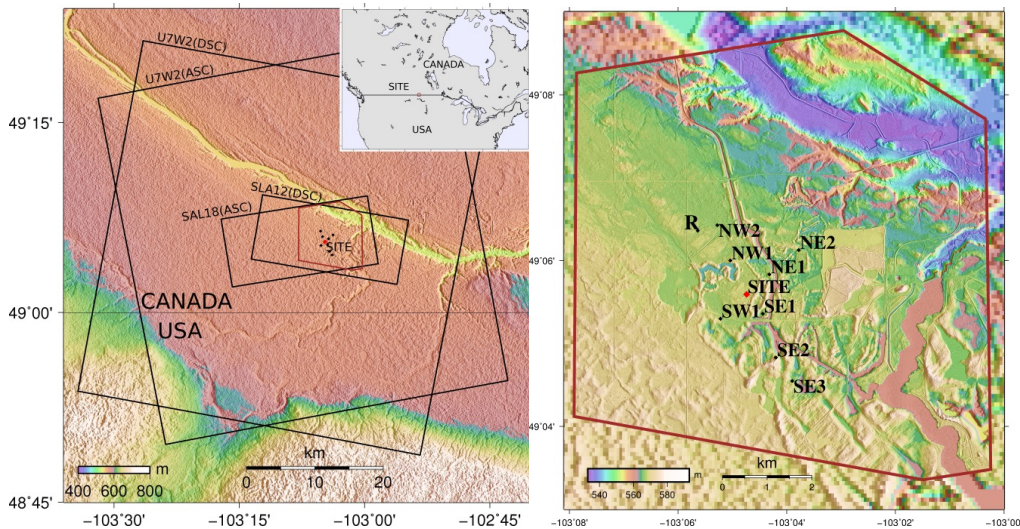

Figure 9: (Left panel) Location of the Aquistore storage site in Saskatchewan, Canada. Advanced Spaceborne Thermal Emission and Reflection Radiometer (ASTER) 30 m resolution Digital Elevation Model (DEM). The RADARSAT-2 InSAR data frames are outlined in black. The region of interest is outlined in brown. Extent in top-right corner shows location of study region in North America. (Right panel) LIDAR 1 m resolution DEM plotted over ASTER DEM. The reference region ``R'' is assumed to be stable. The monitoring sites NE1, NE2, SE1, SE2, SE3, SITE, SW1, NW1, NW2 are plotted in black.

A key objective of the Aquistore project is to integrate numerous data sets in order to determine the subsurface fluid distribution, pressure changes and ground deformation associated with the injection. For

these purposes a variety of surface-based, continuous-recording instruments were installed at the site including Global Navigation Satellite System (GNSS) receivers, tiltmeters, seismographs, and piezometers. Space-borne Differential Interferometric Synthetic Aperture Radar (DInSAR) is used to measure the ground deformation over a large area surrounding the site. Ascending and descending RADARSAT-2 Spotlight and Wide Ultra-Fine SAR data are gathered in order to achieve a high temporal and spatial sampling of the deformation field. The footprints of the SAR images are shown in Figure 9. The Spotlight data consist of ascending descending Spotlight images (Figure 9), acquired with the incidence angles of 44 and 40 degrees and the range-azimuth spatial resolution of 1.6x0.8 m. The Wide Ultra-Fine data consist of both ascending and descending Wide 2 Ultra-Fine images, acquired with an incidence angle of 37 degrees and the range-azimuth spatial resolution of 1.6x2.8 m. Combining the four independent data sets decreases the time between surveys from 24 days to 6 days. A LIDAR digital elevation map with 1 m resolution was used to remove the phase changes due to topography.
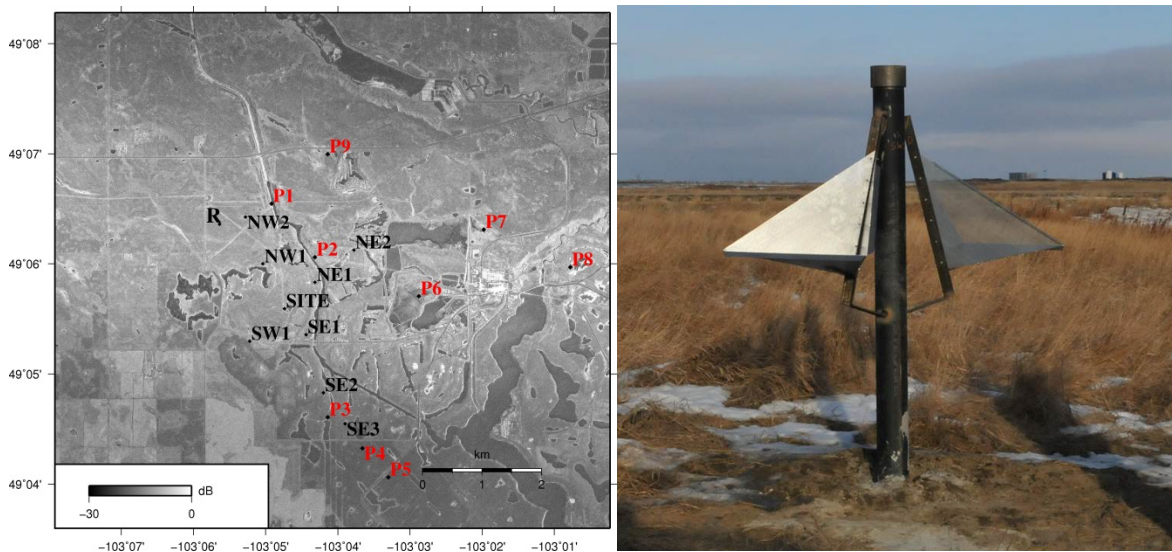

Figure 10. (Left panel) RADARSAT-2 Spotlight 18 SAR intensity image acquired on 8/23/2014. Monitoring sites and stable reference region ``R'' are plotted in black. Points P1-P9 experiencing fast ground deformation are plotted in red. RADARSAT-2 Data. (Right panel) Photograph of corner reflector designed at the Canada Centre for Mapping and Earth Observation, Natural Resources Canada by K. Murnaghan for ascending and descending imaging.

The SAR data are converted to individual interferograms, geocoded, and resampled to a common grid and then processed with the advanced Multidimensional Small Baseline (MSBAS) processor (Samsonov and d'Oreyer, 2011). The MSBAS technique estimates two-dimensional (vertical and East-West) deformation time series, relative to a stable reference point, labeled R in Figures 9 and 10, by combing SAR data from various sensors and acquisition geometries. To further improve the precision of deformation measurements, especially during

the winter months when the ground is covered by snow, a network of corner reflectors was installed with reflectors at nine monitoring sites marked in Figures 9 and 10. The corner reflectors were designed at the Canada Centre for Mapping and Earth Observation, Natural Resources Canada. They consist of two trihedral reflectors positioned for ascending and descending imaging geometry (Figure 10) and mounted on a single monument. In order to more accurately capture ground deformation from a deep source (i.e., CO_2 injection) and to reduce signals from the near surface processes caused by seasonal changes and post-mining soil settlement the corner reflector monuments were anchored at a depth of 20 meters.

RADARSAT-2 SAR data have been collected since June 2012, well before the start of injection in April 2015. The roughly three years of pre-injection observations allowed for the determination of background surface deformation due to variety of sources. The vertical and east-west horizontal deformation maps are shown in Figure 11. During the 2012-2014 period, active ground deformation processes were observed across the region. Subsidence, exceeding 0.8 cm/year, was predominantly observed in areas undergoing mining reclamation and in regions where construction activities have influenced the surface. Uplift was observed at a number of man-made sites, but other locations are affected by groundwater recharge and swelling clays. Horizontal motions of up to 0.4 cm/year were observed, mainly along the steep slopes of the diversion canal. Analysis of the pre-injection deformation reveals that some sites are affected by near-surface deformation processes, in particular sites located south of the injection well (SW1, SE2, SE3), emphasizing the importance of adequate pre-injection monitoring. In Figure 12 we plot the displacement components associated with point P2 in Figure 11, a point close to the injection site that experienced some fast ground deformation.

Elastic and poroelastic modeling was performed to simulate the ground deformation that would be caused by CO_2 injection rates of 1500 tonnes/day (i.e., the maximum expected rate) at a depth of 3150-3350 m (Samsonov et al., 2015). Elastic modeling with a point source model (Mogi, 1958) suggests a constant annual uplift rate of about 1.6 cm/year and east-west motion of up to 0.6 cm/year. However, poroelastic modeling suggests that uplift will reach its maximum value of about 1.6 cm near the injection site almost immediately after the start of injection but its spatial extent will continue to increase during the entire modeled injection period of 25 years. Horizontal motion calculated by the poroelastic model does not exceed 0.1 cm but forms a very broad pattern, extending 40 km from the injection well. The poroelastic model better represents the constitutive properties of the fluid-filled porous rocks and the nature of the injection process, and is considered to be more realistic than the elastic model. Comparison of the poroelastic model predictions of ground deformation with the measurement precision (95% confidence interval) of the deformation maps, which does not exceed 0.3 and 0.2 cm/year, suggests that the horizontal displacements will be smaller than the noise.
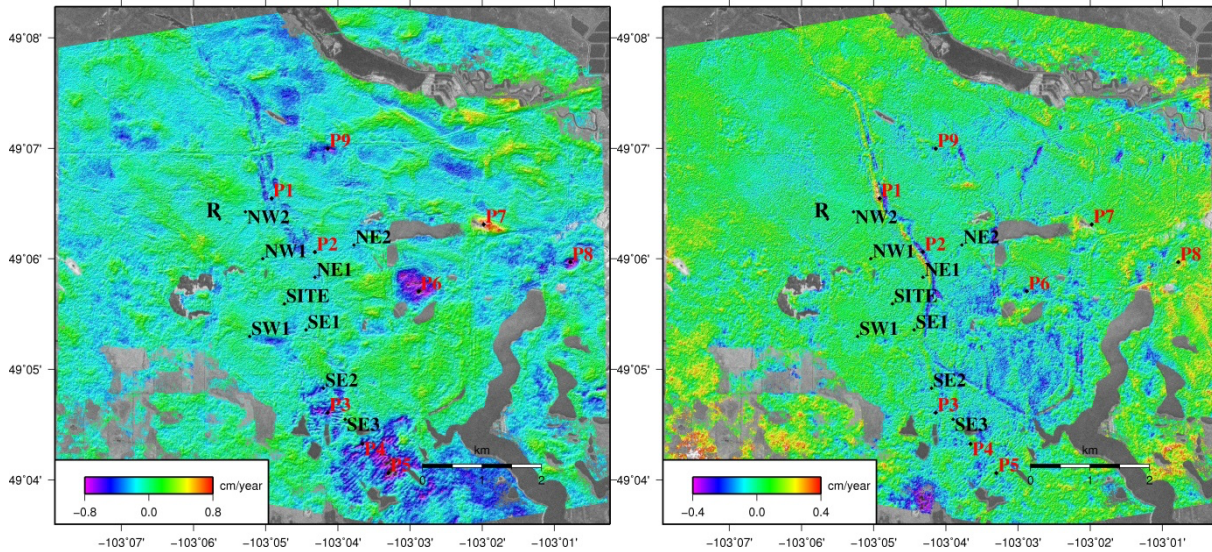
Figure 11. Observed vertical (left) and east-west horizontal (right) deformation rates computed by applying Multidimensional Small Baseline (MSBAS) technique to RADARSAT-2 data spanning a time interval, 6/15/2012 to 9/23/2014, prior to the start of injection. Monitoring sites and reference region ``R'' are plotted in black. Points P1-P9 experiencing fast ground deformation are plotted in red. SAR intensity image is exposed in background in regions of low coherence.
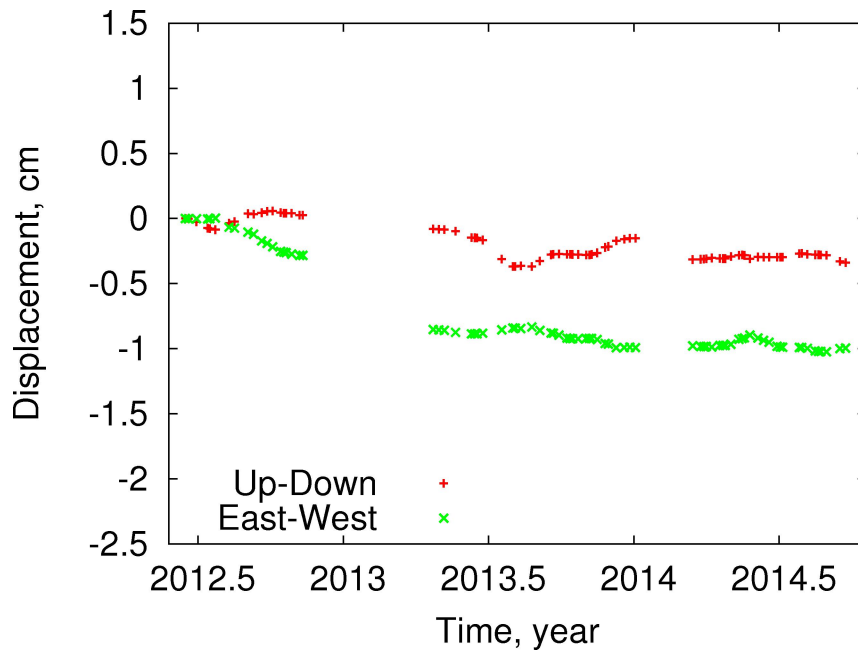

Figure 12. Two components of displacement associated with point P2 from Figure 10. This location is not far from the injection site and has experienced some deformation prior to injection.

Illinois Basin Decatur Project, USA

The Illinois Basin Decatur project, started in November 2011, is a multi-year program managed by Archer Daniels Midland, the U. S. Department of Energy, the Illinois State Geological Survey, and Schlumberger Carbon Services. This is the only carbon capture and storage effort in the United States that is currently injecting large volumes of greenhouse gas emissions into a regional deep saline formation (Finley et al. 2011, 2013). The injection, from an ethanol production facility, started at a rate of 1000 metric tons/day and is planned to increase to over 2000 metric tons/day. The super-critical carbon dioxide is stored in the 550 m thick Mount Simon sandstone at a depth of 2.1 km. The overlying Eau Claire shale forms a 100 to 150 m thick seal. The Mount Simon formation was the site of a functioning natural gas storage facility and has performed well in that capability. Several different geochemical, geophysical, and remote sensing technologies are employed at the site to monitor the evolution of the injected volume of carbon dioxide. Preliminary results from micro-seismic and InSAR monitoring have been reported by Kaven et al. (2014) and Falorni et al. (2014), respectively.

The injection site is situated in a mixture of industrial sites, farmland, forest, and residential areas and InSAR monitoring can be challenging in such a diverse environment. The SqueeSAR algorithm described in the Methodology section, with its combination of permanent or persistent scatterers (PS) and distributed scatterers (DS), is a flexible method for treating such a wide variety of land surfaces. The distribution of the approximately 109,000 scatterers found in the region surrounding the injection well (Falorni et all 2014) is shown in Figure 13.
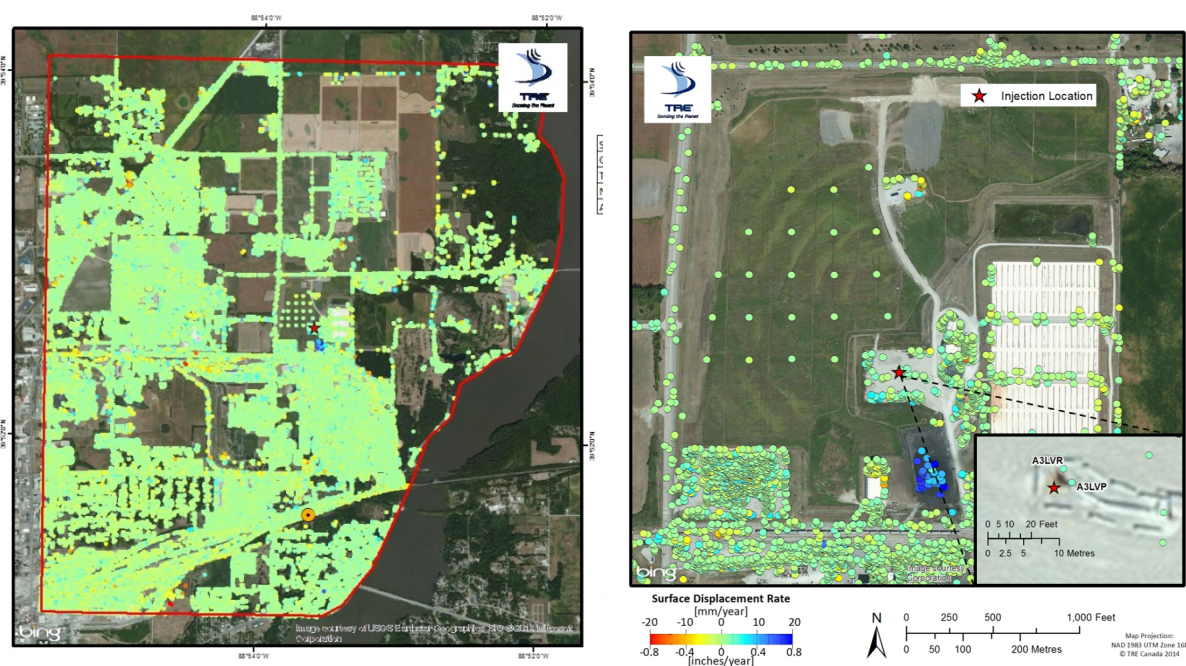
Figure 13: (Left panel) Distribution of scatterers in the region surrounding the injection well (magenta star), roughly 4000 per square kilometer. (Right panel) Close-up view of the region surrounding the injection well-pad. The grid of artificial reflectors is visible to the northwest of the well-head.

Another difficulty is introduced by the seasonal and atmospheric conditions, including long periods of snow cover in this part of the world. Some permanent scatterers such as steep roofs and tall towers may not accumulate much snow, but large areas will be covered, reducing the coherence and introducing significant variations the characteristics of the scattering surface. Artificial reflectors, man-made, stable targets designed to remain free of snow, are one remedy and are commonly used in areas prone to snowfall. In order to provide for year-round coverage, 21 artificial reflectors, spaced 75 m apart, were constructed and emplaced in an open area close to the injection well-pad (Figure 13). All 21 reflectors were found to have strong and stable reflectivity, both for ascending and descending satellite orbits.
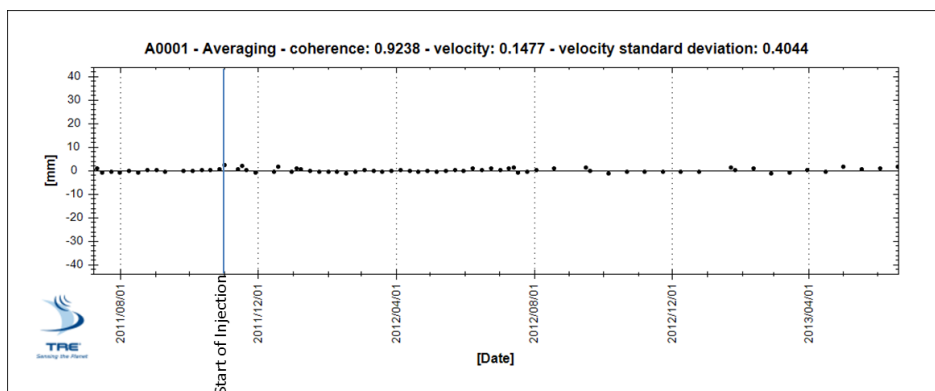

Figure 14: Average range change from the 21 artificial reflectors installed just to the northwest of the injection well site (Falorni et al. 2014). The start of injection is indicated by the vertical blue line.

The acquisition of COSMO-SkyMed X-band data began in July 2011, before the start of injection in November. Falorni et al. (2014) have reported on roughly two years of observations from July 2011 until June 2013. They note that there is little or no ground motion associated with the start of injection with the exception of two points. For example, a time series consisting of the average range change from all 21 reflectors is plotted in Figure 14. The two points showing some movement correlating with the start of injection were in the vicinity of the injection well and may reflect some movement related to the pressurization of the well bore itself (Figure 15).
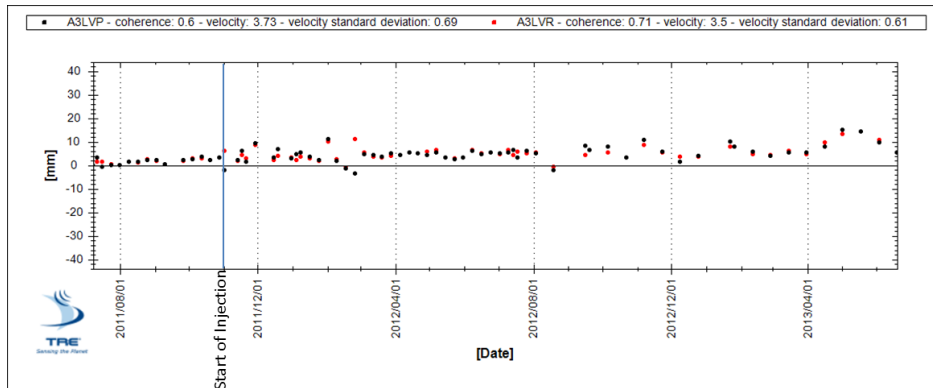
Figure 15. Time series of two measurement points in the vicinity of the injection well. The vertical blue line indicates the start of injection.

The lack of injection-related surface deformation is an expected result. Due to the high permeability and thickness of the reservoir sandstone, the bottom hole pressure has changed very little during the injection. Barring any unforeseen geologic features, such as an unmapped fracture zone, the carbon dioxide is expected to migrate outward into the reservoir without generating a large pressure change and associated deformation. The InSAR observations serve to verify the expected performance of the sequestration effort and to detect any deformation that may imply the upward movement of the carbon dioxide.

Conclusions

Geodetic methods are well suited for monitoring the effectiveness of the geological storage of carbon dioxide. The application to carbon sequestration is still relatively new, but approaches such as Interferometric Synthetic Aperture Radar appear promising even at sites subject to periodic snow cover. Enhancements, such as artificial radar reflectors may be required for certain difficult terrains such as farmed fields with intermittent snow cover. Even in these difficult areas it appears possible to monitor ground deformation with the accuracy of 0.5 cm. In favorable regions such as desert regions with little movable sand, the accuracy can be of the order of a few millimeters. In an application at In Salah, Algeria, InSAR appears to be sensitive to focused flow in a narrow higher permeability damage zone, indicating deviations from pure reservoir flow. Other geodetic techniques, such as tilt meters, the Global Positioning System (GPS), and Laser ranging (LiDAR) are also possible. Some methods, such as precision bathymetry and time-lapse seismic strain measurements (Rickett et al. 2007) are applicable to storage in deformable offshore reservoirs.

References

Aki, K. and Richards, P. G., (1980). *Quantitative Seismology*, W. H. Freeman and Company.

Bissell, R. C., Vasco, D. W., Atbi, M., Hamdani, M., Okwelegbe, M., and Goldwater, M. H. (2010). A full field simulation of In Salah Gas production and CO2 storage project using coupled geo-mechanical and thermal fluid flow simulator, *Energy Procedia*, **4**, 3290-3297.

Davis, P. M., (1983). Surface deformation associated with a dipping hydrofracture, *Journal of Geophysical Research*, **88**, 5826-5834.

Chawah, P., Chery, J. Boudin, F., Cattoen, M. Seat, H. C., Plantier, G., Lizion, F. Sourice, A., Bernard, P, Brunet, C., Boyer, D., and Gaffet, S., (2015). A simple pendulum borehole tiltmeter based on a triaxial optical-fibre displacement sensor, *Geophysical Journal International*, **203**, 1026-1038, https://doi.org/10.1093/gji/ggv358

Eitel, J. J. H., Hofle, B., Vierling, L. A., Abellan, A., Asner, G. P., Deems, J. S, Glennie, C. L., Joerg, P. C., LeWinter, A. L., Magney, T. S., Mandlburger, G., Morton, D. C., Muller, J., and Vierling, K. T. (2016). Beyond 3-D: The new spectrum of lidar applications for earth and ecological sciences, *Remote Sensing of Environment*, **186**, 372-392.

Falorni, G, Hsiao, V., Iannaconne, J., Morgan, J., and Michaud, J.-S. (2014.) InSAR monitoring of ground deformation at the Illinois Basin Decatur Project, in Carbon Dioxide Capture for Storage in Deep Geological Formations, Volume **4**, CPL Press.

Ferretti, A., Monti-Guarnieri A., Prati, C., Rocca, F., Massonnet, D. (2007a). *InSAR Principles: Guidelines for SAR Interferometry Processing and Interpretation*. ESA Publications, TM-19. ISBN 92-9092-233-8. Available at: http://www.esa.int/About_Us/ESA_Publications

Ferretti, A., Prati, C. and Rocca, F. (2000). Nonlinear subsidence rate estimation using permanent scatterers in differential SAR interferometry. *IEEE Transactions on Geoscience and Remote Sensing*, **38**(5), 2202-2212.

Ferretti, A., Prati, C. and Rocca, F. (2001). Permanent Scatterers in SAR Interferometry, *IEEE Transactions on Geoscience and Remote Sensing*, **39**(1), 8 -20.

Ferretti, A., Fumagalli, A., Novali, F., Prati, C., Rocca, F. and Rucci, A. (2011). A new algorithm for processing interferometric data-stacks: SqueeSAR. *IEEE Transactions on Geoscience and Remote Sensing*, **49**(9), 3460-3470.

Ferretti, A. (2014). *Satellite InSAR Data – Reservoir Monitoring from Space*. EAGE Publications.

Finley, R. J., Greenberg, S. D., Frailey, S. M., Krapac, I. G., Leetaru, H. E., and Marsteller, S. (2011). The path to a successful one-million tonne demonstration of geological sequestration: characterization, cooperation, and collaboration, *Energy Procedia*, **4**, 4770-4776.

Finley, R. J., Frailey, S. M., Leetaru, H. E., Senel, O., Coueslan, M. L., and Marsteller, S. (2013). Early operational experience at a one-million tonne CCS demonstration project, Decatur, Illinois, *Energy Procedia*, **37**, 6149-6155.

Gibson-Poole, C. M., and Raikes, S., (2010). Enhanced understanding of CO_2 storage at Krechba from 3D seismic, in *Proceedings of the 9th Annual Conference on Carbon Capture and Sequestration*, Pittsburgh, PA, May 10-13, 2010.

Hisz, D. B., Murdoch, J. C., and Germanovich, L. N. (2013). A portable extensometer and tiltmeter for characterizing aquifers, Water Resources Research, 49, 7900-7910. https://doi.org/10.1002.wrcr.20500

Joyce, K. E., Samsonov, S. V., Levick, S. R., Engelbrecht, J. and Belliss, S. (2014). Mapping and monitoring geological hazards using optical, LiDAR, and synthetic aperture RADAR image data, *Natural Hazards*, **73**, 137-163.

Kaven, J. O., Hickman, S. H., McGarr, A. F., Walter, S., and Ellsworth, W. L. (2014).Seismic monitoring at the Decatur, IL, CO_2 sequestration demonstration site, *Energy Procedia*, **63**, 4264-4272.

Massonnet, D., and Feigl, K. L. (1998). Radar interferometry and its applications to changes in the Earth's surface, *Reviews of Geophysics*, **36**, 441-500.

Mathieson, A. Midgley, J., Dodds, K., Wright, I., Ringrose, P., and Saoula, N. (2010). CO2 sequestration monitoring and verification technologies applied at Krechba, Algeria, *The Leading Edge*, **29**, 216-222.

Mathias, S., Hardisty, P., Trudell, M., Zimmerman, R., (2009). Approximate solutions for pressure buildup during CO2 injection in brine aquifers. *Transport in Porous Media*, **79**, 265-284.

Mogi, K., (1958). Relations between the eruptions of various volcanoes and the deformation of the ground surfaces above them, *University of Tokyo Earthquake Research Institute Bulletin*, **36**, 99-134.

Moreau, F, and Dauteuil, O. (2013). Geodetic tools for hydrogeological surveys: 3D-displacements above a fractured aquifer from GPS time series, *Engineering Geology*, **152**, 1-9.

Norford, B., Haidl, R., Bezys, F.M., Cecile, M., McCabe, H., Paterson, D. (1994). Middle Ordovician to Lower Devonian strata of the Western Canada Sedimentary Basin. In: Mossop, G., I.S. (comp. (Eds.), Geological Atlas of the Western Canada Sedimentary Basin. Canadian Society of Petroleum Geologists, Calgary, Alberta and Alberta Research Council, Edmonton, Alberta, pp. 109-127.

Rickett, J., Duranti, L., Hudson, T., Regel, B., and Hodgson, N., (2007). 4D time strain and the seismic signature of geomechanical compaction at Genesis, *The Leading Edge*, **26**, 644-647.

Ringrose, P. S., Mathieson, A. S., Wright, I. W., Selama, F., Hansen, O., Bissell, R., and Midgley, J. (2013). The In Salah CO2 storage project: lessons learned and knowledge transfer, *Energy Procedia*, **37**, 6226-6236.

Rosen, P., Hensley S., Joughin I., Li F., Madsen S.N., Rodriguez E., Goldstein R. (2000). Synthetic Aperture Radar Interferometry. *Proceedings of the IEEE*, **88**(3), 333-382.

Rucci, A., Vasco, D. W. and Novali, F. (2010). Fluid pressure arrival-time tomography: Estimation and assessment in the presence of inequality constraints with an application to production in the Krechba field, Algeria. *Geophysics*, **75**, O39-O55.

Rucci, A., Vasco, D. W. and Novali, F. (2013). Monitoring the geologic storage of carbon dioxide using multicomponent SAR interferometry. *Geophysical Journal International*, **193**(1), 197-208.

Samsonov, S., d'Oreye, N. (2012). Multidimensional time series analysis of ground deformation from multiple InSAR data sets applied to Virunga Volcanic Province. Geophys. J. Int. 191, 1095-1108, http://dx.doi.org/10.1111/j.1365-246X.2012.05669.x.

Samsonov, S., Czarnogorska, M., White, D. (2015), Satellite interferometry for high-precision detection of ground deformation at a carbon-dioxide storage site, *International Journal of Greenhouse Gas Control*, **42**, 188-199.

Schuite J., Longuevergne, L., Bour, O., Burbey, T. J., Boudin, F., Lavenant, N. and Davy, P. (2017). Understanding the hydromechanical behavior of a fault zone from transient surface tilt and fluid pressure observations at hourly time scales, *Water Resources Research*, **53**, 10558-10582, https://doi.org/10.1002/2017WR020588.

Vasco, D. W., (2004). Estimation of flow properties using surface deformation and head data: A trajectory-based approach, *Water Resources Research*, **40**, 1-14, http://dx.doi.org/10.1029/2004WR003272.

Vasco, D. W., and Datta-Gupta, A. (2016). *Subsurface Fluid Flow and Imaging*, Cambridge University Press, Cambridge.

Vasco, D. W., Johnson, L. R., and Goldstein, N. E., (1988). Using surface deformation and strain to determine deformation at depth, with an application to Long Valley, Caldera, California, *Journal of Geophysical Research*, **93**, 3232,3242.

Vasco, D. W., Karasaki, K., and Keers, H., (2000). Estimation of reservoir properties using transient pressure data: An asymptotic approach, *Water Resources Research*, **36**, 3447-3465, http://dx.doi.org/10.1029/2004WR003272.

Vasco, D. W., Ferretti, A., and Novali, F., (2008), Estimating permeability from quasi-static deformation: Temporal variations and arrival time inversion, *Geophysics*, **73**, O37-O52, doi:10.1190/1.2978164.

Vasco, D. W., Rucci, A., Ferretti, A., Novali, F., Bissell, R. C., Ringrose, P. S., Mathieson, A. S., and Wright, I. W., (2010), Satellite-based measurements of surface deformation reveal fluid flow associated with the geological storage of carbon dioxide, *Geophysical Research Letters*, **37**, L03303, 1-5, doi:10.1029/2009GL041544.

Wang, R., Lorenzo-Martin, F. and Roth, F., (2006). PSGRN/PSCMP – a new code for calculating co- and post-seismic deformation, geoid and gravity changes based on the viscoelastic-gravitational dislocation theory, *Comput Geosci.,* **32**, 527-541.

Worth, K., White, D., Chalaturnyk, R., Sorensen, J., Hawkes, C., Rostron, B., Johnson,J., Young, A., (2014). Aquistore project measurement, monitoring and verification: from concept to CO2 injection. *Energy Procedia*, **63**, 3202-3208, http://dx.doi.org/10.1016/j.egypro.2014.11.345.

Wright, C. A., (1998). Tiltmeter fracture mapping: From the surface and now downhole, *Petrol. Eng. Int*., **71**, 50-63.

Xu, Z., Fang, Y., Scheibe, T., Bonneville, A., (2012). A fluid pressure and deformation analysis for geological sequestration of carbon dioxide. *Computational Geosciences*, **46**, 31-37.

Zhang, R. Vasco, D. W., Daley, T. M., and Harbert, W., (2015). Characterization of a fracture zone using seismic attributes at the InSalah CO2 storage project, *Interpretation*, May, SM37-SM46, doi:10.1190/INT-2014-0141.1.

Zhang, R., Vasco, D. W., and Daley, T. M., (2016). Study of seismic diffraction wave caused by a fracture zone at the InSalah carbon dioxide storage project, *International Journal of Greenhouse Gas Control*, **42**, 75-86, doi:10.1016/j.i.jggc.2015.07.033.